Supporting Information

TITLE. Mid-Infrared InAs/InAsSb Superlattice nBn Photodetector Monolithically Integrated onto Silicon

AUTHORS. Evangelia Delli[1*], Veronica Letka[2], Peter D. Hodgson[2], Eva Repiso[2], Jonathan P. Hayton[1], Adam P. Craig[2], Qi Lu[2], Richard Beanland[3], Anthony Krier[2], Andrew R. J. Marshall[2] and Peter J. Carrington[1*]

[1]Engineering Department, Lancaster University, Bailrigg, Lancaster, LA1 4YW, UK

[2]Physics Department, Lancaster University, Bailrigg, Lancaster, LA1 4YB, UK

[3] Physics Department, University of Warwick, Coventry, CA4 7AL, UK

NUMBER OF PAGES. 11

NUMBER OF FIGURES. 6

NUMBER OF TABLES. 1

Characterization of GaSb/Si buffer

Si substrate. Figure S1 shows a high-resolution transmission electron microscopy (TEM) micrograph of the Si:III-V interface, which allows the direct observation of the atomic configuration and confirms the 4° offcut of Si surface towards [0-11] directions.
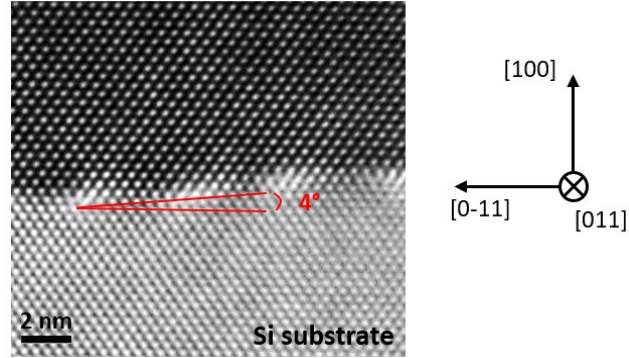

Figure S1. High resolution bright field TEM micrograph of Si:III-V interface.
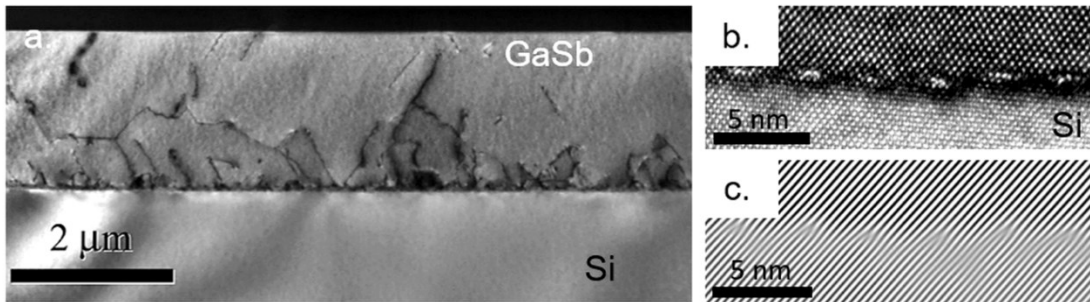

Figure S2. (a) Dark field TEM image of the two-step GaSb buffer layer taken along the [220] direction. (b) High resolution TEM image of the Si:III-V interface presenting the well-formed IMF array. (c) Fourier filter image of the IMF array shown in Fig. (b) obtained using (-111) Bragg reflection.

Two-step growth temperature GaSb buffer. Figure S2 (a) shows a TEM image of the 2 μm thick two-step GaSb buffer layer. The threading dislocation density significantly decreased within the first half of the buffer layer and no APDs were observed, contrary to previous reports[1]. The high resolution TEM image in Fig. S2 (b) shows the periodic arrangement of the interfacial misfit dislocations (IMFs) network at the Si:III-V interface. Fourier filtering using the (-111) Bragg reflection was employed to highlight the IMFs position and the extra atomic planes on the Si side as shown in Fig. S2 (c).
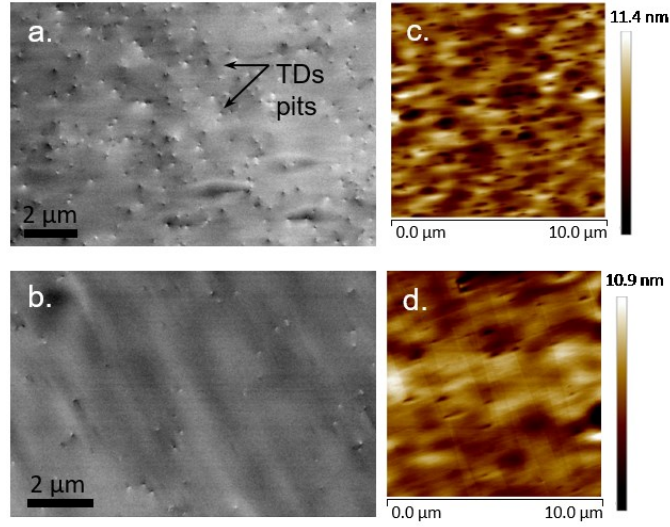

Figure S3. ECCI surface images of samples grown using (a) just the two-step GaSb buffer and (b) the two-step buffer and DFs. AFM surface images of (c) the two step-buffer and (d) the DF sample.

Dislocation filters. Figure S3 presents a surface comparison using electron channeling contrast imaging ECCI and AFM: of the two-step GaSb buffer layer and the improvements observed with the dislocation filters (DFs). A resulting root mean square (RMS) surface roughness of 2 nm (AFM: area: 10 x 10 μm) was measured from the two-step GaSb buffer layer and a threading

dislocation pit density of 2 x 10^8 cm^{-2}. The use of DFs reduced the surface roughness to 1.18 nm

and the dislocation density to 3 x 10^7 cm^{-2}. This RMS surface roughness is lower than previously

reports on GaSb/Si[2] and close to values reported for GaSb integrated onto lower lattice mismatched
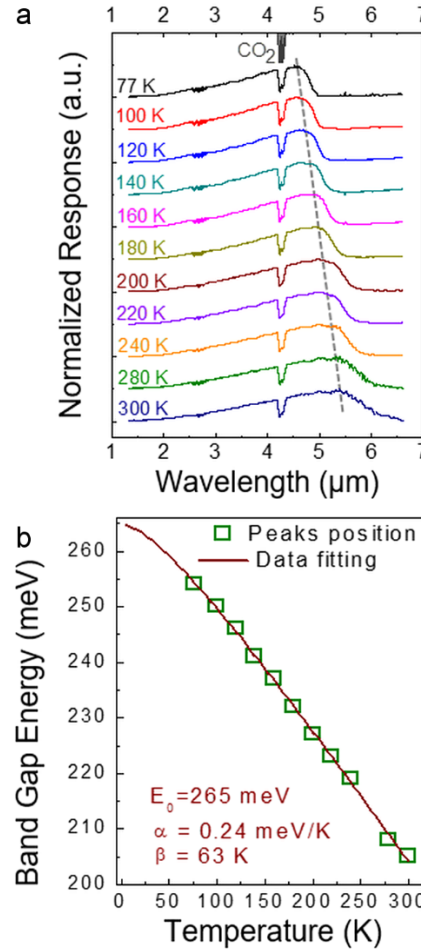
GaAs[3].

Figure S4. (a) Normalized spectral response signal of the SL nBn detector obtained at different

temperatures. (b) Peak response energy dependence on temperature with a Varshni line of best fit.

Temperature dependent spectral response

The temperature dependent spectral response is shown in Figure S4 (a). An absorption dip due to CO_2 can be clearly observed, while the 50% cut-off wavelength red shifts towards longer wavelengths with increasing temperature. Plotting the square of the response at each temperature against the energy and extrapolating to the zero value reveals information on the energy gap[4], as shown in Figure S4 (b). The data is fit using the Varshni equation[5]

$$E_g(T) = E_0 - \frac{aT^2}{\beta+T} \tag{1}$$

where E_0 (eV) is the band gap at 0 K, α and β are Varshni coefficients and T is the temperature in Kelvin. A 0 K ground-state transition energy of $E_0 = 265$ meV was found, which is in agreement with the 268 meV ground-state recombination calculated using *Nextnano*. The constants α and β were found to be 0.24 meV/K and 63K respectively.

Designing a strain balanced type-II InAs/InAsSb SL

To achieve a high quality InAs/InAsSb SL it is important to accomplish strain balancing on GaSb using an optimized combination of layer thicknesses and Sb composition in the InAsSb layer. Furthermore, as the layers of the SL are strained the thickness of every single layer needs to be smaller than the critical thickness, equal to 20 nm for the InAs/GaSb system as predicted using the classic Matthews-Blakeslee model[6]. The strain balancing conditions for the InAs/InAsSb SL on GaSb can be described using the equation[7]

$$t_{InAsSb} = \left(\frac{a_{GaSb}-a_{InAs}}{a_{InSb}-a_{InAs}}\right)\left(\frac{P}{x}\right) = 0.090\left(\frac{P}{x}\right) \tag{2}$$

where $P = t_{InAs} + t_{InAsSb}$ is the thickness of one period, t_i is the thickness of the i-th layer, x is the fraction of Sb in the InAsSb layer and a_i is the lattice constant of the i-th material. An Sb content of 16% and a period of P= 13.3 nm was chosen to tune the SL emission wavelength over the 3 – 5 μm atmospheric window resulting in t_{InAs} = 7.4 nm and t_{InAsSb} = 5.9 nm.

The band structure and the quantum confined bands inside the InAs/InAsSb type-II SL were calculated using a six-band k·p solver using *Nextnano* software[8]. Material parameters for the bulk InAs and InSb were taken from the work reported by *Vurgaftman et al*[9]. The lattice constant of InAsSb alloys were obtained using Vegard's law

$$a(InAs_{1-x}Sb_x) = xa(InSb) + (1 - x)a(InAs) \tag{3}$$

by interpolation of values between InAs and InSb binary alloys. The band gap energy E_g was obtained using the quadratic approximation

$$E_g(InAs_{1-x}Sb_x) = xE_g(InSb) + (1 - x)E_g(InAs) + x(1 - x)C \tag{4}$$

where C is the bowing parameter for InAsSb. A value of 0.971 eV was used for the total bowing parameter, as reported by *Webster et. al.*[10] The predicted transition energy from the conduction band to the lowest confined heavy hole level in the InAsSb well was in excellent agreement with the experimental photoluminescence and spectral response results.

Overview and summary of recent results

Figure S5 and S6 presents an overview of the specific detectivity (D*) and external quantum efficiency (EQE) results from this work along with previously published data for state-of-the-art photodetector devices (References No. 11 - 21). All detector devices show a mid-wavelength infrared 50% cut-off wavelength. These results are comparable to that of type-II superlattice pin

detectors integrated on GaSb[11,15,16,20] and GaAs[11] substrates which can be attributed to the excellent crystal quality of the GaSb-on-Si buffer layer. Further optimization of the GaSb buffer could lead to further improvements, paving the way for future high temperature and performance Si integrated devices, comparable to those of state-of-the-art InAs/GaSb SL pMp detector structures[13,21]. Table S1 also presents a summary of D* and EQE for recent devices operating in the mid-infrared spectral region.

Table S1. Key operating parameters (D* and EQE) of detector devices reported previously in the literature.

| Structure	50% cut-off wavelength (µm)	D* (Jones)	EQE (%)	Temperature (K)
InAs/GaSb SL pin on GaSb [11]	3.7	4.7×10^{10}	-	80
InAs/GaSb SL pin on GaAs [11]	3.7	2.34×10^{10}	-	80
InAs/GaSb SL p-on-n on GaSb [12]	4.5	2×10^{9}	8	240
InAs/GaSb SL pMp on GaSb [13]	4.4	8×10^{11}	44	150
InSb pin on Si [14]	5.3	8.8×10^{9}	16.3	80
InAs/GaSb SL pin on GaSb [15]	5.4	3×10^{12}	25	77
InAs/InAsSb SL pin on GaSb [16]	5	-	24.1	80
InSb pin on Si [17]	5.3	3.08×10^{9}	11.1	77
InGaAs/InAsSb SL nBn on GaSb [18]	3.4	-	27	180
InAs/GaSb SL pBiBn on GaSb [19]	4.2	2.1×10^{11}	38	77
InAs/InAsSb SL pin on GaSb [20]	5.4	-	20	77
InAs/GaSb SL pMp on GaSb [21]	4.5	7.7×10^{9}	68.6	250
InAs/InAsSb SL nBn on Si [This work]	5.4	3.65×10^{10}	25.6 (200K)	160
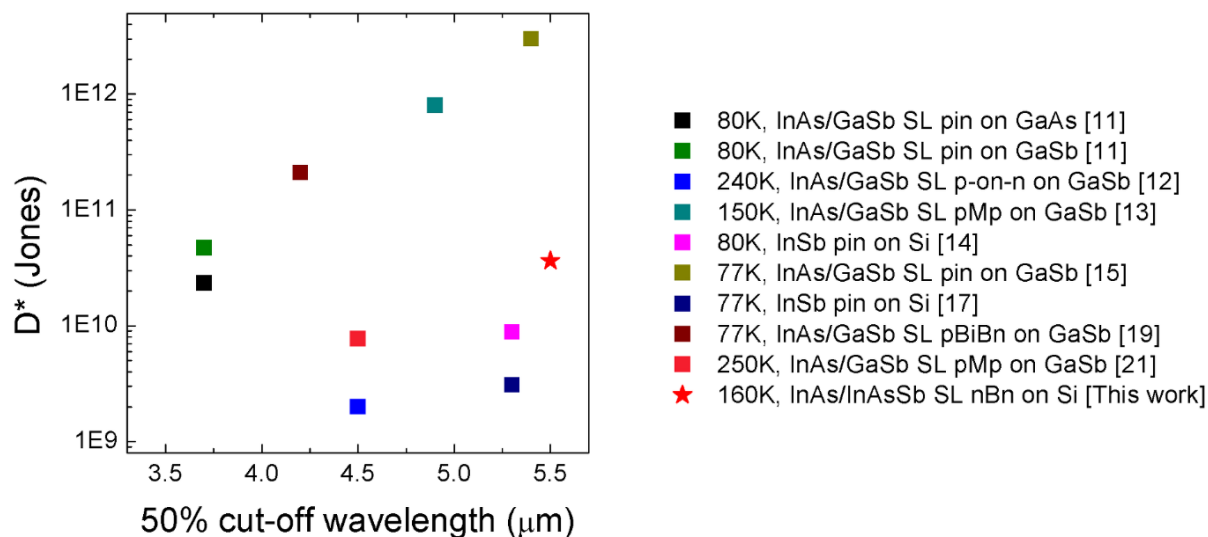
Figure S5. Summary of recent results showing the specific detectivity as a function of the cut-off wavelength.
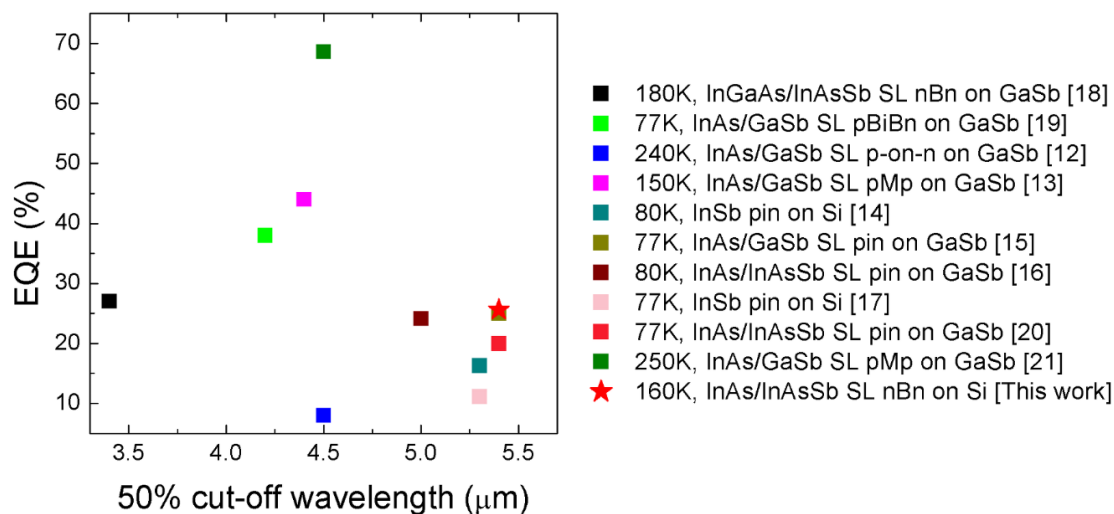

Figure S6. Summary of recent results showing the external quantum efficiency as a function of the cut-off wavelength.

AUTHOR INFORMATION

Corresponding Author

*E-mail: e.delli@lancaster.ac.uk.

*E-mail: p.carrington@lancaster.ac.uk.

REFERENCES

(1) Woo, S. Y.; Hosseini Vajargah, S.; Ghanad-Tavakoli, S.; Kleiman, R. N.; Botton, G. A.; Direct observation of anti-phase boundaries in heteroepitaxy of GaSb thin films grown on Si (001) by transmission electron microscopy. *J. Appl. Phys.* 2012, 112, 074306.

(2) Rodriguez, J. B.; Madiomanana, K.; Cerutti, L.; Castellano, A.; Tournié E. X-ray diffraction study of GaSb grown by molecular beam epitaxy on silicon substrates. *J. Cryst. Growth* 2016, 439, 33-39.

(3) Mansoori, A.; Addamane, S. J.; Renteria, E. J.; Shima, D. M.; Behzadirad, M.; Vadiee, E.; Honsberg, C.; Balakrishnan, G. Reducing threading dislocation density in GaSb photovoltaic devices on GaAs by using AlSb dislocation filtering layers. *Solar En. Mater. and Solar Cells* 2018, 185, 21-27.

(4) Craig, A. P.; Jain, M.; Wicks, G.; Hossain, K.; McEwan, K.; Howle, C.; Percy, B.; Marshall, A. R. J. Short-wave infrared barriode detectors using InGaAsSb absorption material lattice matched to GaSb. *Appl. Phys. Lett.* 2015, 106, 201103.

(5) Ning, Z. -D.; Liu, S. -M.; Luo, S.; Ren, F.; Wang, F.; Yang, T.; Liu, F. -Q.; Wang, Z. -G.; Zhao, L. -C. Structural and optical properties of InAs/InAsSb superlattices grown by metal

organic chemical vapor deposition for mid-wavelength infrared photodetectors. *Appl. Surface Science* 2016, 368, 110-113.

(6) Matthew, J. B.; Blakeslee, A.E. Defects in epitaxial multilayers: I. Misfit dislocations. *J. Cryst. Growth* 1974, 27, 118-125.

(7) Lackner, D. InAsSb/InAs strain balanced superlattices for photodetector applications. *In Phd thesis*, Simo Fraser University, 2011.

(8) https://www.nextnano.de/index.php

(9) Vurgaftman, I.; Meyer, J. R.; Ram-Mohan, L. R. Band parameters for III-V compound semiconductors and their alloys. *J. Appl. Phys.* 2001, 89, 5815.

(10) Webster, P. T.; Riordan, N. A.; Liu, S.; Steenbergen, E. H.; Synowicki, R. A. Measurement of InAsSb bandgap energy and InAs/InAsSb band edge positions using spectroscopic ellipsometry and photoluminescence spectroscopy. *J. Appl. Phys.* 2015, 118, 245706.

(11) Korkmaz, M.; Arikan, Bulent.; Suyolcu, Y. E.; Aslan, B.; Serincan, U. Performance evaluation of InAs/GaSb superlattice photodetector. *Semicond. Sci, Technol.* 2018, 33, 035002.

(12) Plis, E.; Rodriguez, J. B.; Kim, H. S.; Bishop, G.; Sharma, Y. D.; Dawson, L. R. Type II InAs/GaSb strain layer superlattice detectors with p-on-n polarity. *Appl. Phys. Lett.* 2007, 91, 133512.

(13) Nguyen, B. -M.; Chen, G.; Hoang, A. M.; Abdollahi Pour, S.; Bogdanov, S.; Razeghi, M. Effect of contact doping in superlattice-based minority carrier unipolar detectors. *Appl. Phys. Lett.* 2011, 99, 033501.

(14) Jia, B. W.; Tan, K. H.; Loke, W. K.; Wicaksono, S.; Lee, K. H.; Yoon, S. F. Monolithic integration of InSb photodetector on Silicon for mid-infrared silicon photonics. *ACS photonics* 2018, 5, 4, 1512-1520.

(15) Chen, J.; Zhou, Y.; Xu, Z.; Xu, J.; Xu, Q.; Chen, H.; He, L. InAs/GaSb type-II superlattice mid-wavelength infrared focal plane array detectors grown by molecular beam epitaxy. *J. Cryst. Growth* 2013, 378, 596-599.

(16) Schuler-Sandy, T.; Klein, B.; Casias, L.; Mathew, S.; Kadlec, C.; Tian, Z.; Plis, E.; Myers, S.; Krishna, S. Growth of InAs-InAsSb SLS through the use of digital alloys. *J. Cryst. Growth* 2015, 425, 29-32.

(17) Jia, B. W.; Tan, K. H.; Loke, W. K.; Wicaksono, S.; Yoon, S. F. Integration of an InSb photodetector on Si via heteroepitaxy for the mid-infrared wavelength region. *Optic Express* 2018, 26, 6.

(18) Ariyawansa, G.; Reyner, C. J.; Duran, J. M.; Reding, J. D.; Scheihing, J. E.; Steenbergen, E. H. Unipolar infrared detectors based on InGaAs/InAsSb ternary superlattices. *Appl. Phys. Lett.* 2016, 109, 021112.

(19) Gautam, N.; Myers, S.; Barne, A. V.; Klein, B.; Smith, E. P.; Rhiger, D. R.; Kim, H. S.; Tian, Z. -B.; Krishna, S. Barrier engineered infrared photodetectors based on type-II InAs/GaSb strained layer superlattices. *IEEE J. Quantum Electronics* 2013*,* 49, 2.

(20) Schuler-Sandy, T.; Myers, S.; Klein, B.; Gautam, N.; Ahirwar, P.; Tian, Z. -B.; Rotter, T.; Balakrishnan, G.; Plis, E.; Krishna, S. Gallium free type II InAs/InAs$_x$Sb$_{1-x}$ superlattice photodetectors. *Appl. Phys. Lett.* 2012, 101, 071111.

(21) Chen, G.; Haddadi, A.; Hoang, A. -M.; Chevallier, R.; Razeghi, M. Demonstration of type II superlattice MWIR minority carrier unipolar imager for high operation temperature application. *Optics Letters* 2015, 40, 1.